EDGE ARTICLE

CrossMark
click for updates

Four-step iron(II) spin state cascade driven by antagonistic solid state interactions†

Natasha F. Sciortino,[a] Katrina A. Zenere,[a] Maggie E. Corrigan,[a] Gregory J. Halder,[b] Guillaume Chastanet,[c] Jean-François Létard,[c] Cameron J. Kepert*[a] and Suzanne M. Neville*[a]

A four-stepped cascade of Fe(II) high spin (HS) to low spin (LS) states is demonstrated in a family of 2-D Hofmann materials, $[Fe_3^{II}(saltrz)_6(M^{II}(CN)_4)_3] \cdot 8(H_2O)$ (M^{II} = Pd (**1**^{Pd}), Pt (**1**^{Pt}); saltrz = (*E*)-2-(((4*H*-1,2,4-triazol-4-yl)imino)methyl)phenol). Alongside the fully HS and LS Fe(II) states, fractional spin state stabilization occurs at HS/LS values of 5/6, 2/3, and 1/6. This unconventional spin state periodicity is driven by the presence of multiple spin crossover (SCO) active Fe(II) sites which are in subtly distinct environments driven by a network of antagonistic host–host and host–guest interactions. Alternating long- and short-range magnetostructural ordering is achieved over the five distinct spin state ratios $HS^{1.0}LS^{0.0}$, $HS^{0.833}LS^{0.167}$, $HS^{0.667}LS^{0.333}$, $HS^{0.167}LS^{0.833}$, and $HS^{0.0}LS^{1.0}$ owing to the flexibility of this 2-D interdigitated lattice topology interconnected by intermolecular interactions. A distinct wave-like spin state patterning is structurally evidenced for each intermediate phase.

Introduction

An alluring aspect of the spin crossover (SCO) phenomenon is its representation of an electronic switch, whereby two distinct magnetic states (high spin (HS) and low spin (LS)) are accessed through variations in environmental factors such as temperature, pressure and light-irradiation.[1–9] The dynamic conversion between these states provides a multitude of physical, chemical and electronic variations with which to target potential applications in the data storage and display device arenas.[2,3,10]

An intriguing characteristic of the SCO effect is the cohort of short- and long-range lattice effects which enable solid state cooperativity, reflected by hysteretic and multi-stepped spin transitions.[10,11] Multi-stepped spin transitions arise from competing "ferro- and "antiferro-elastic-like interactions and are pursued both fundamentally and with an interest in exploring their novel electronic functionalities for applications such as in ternary and higher-order information storage. In that sense, elastic frustration is of primordial importance to induce multi-stepped character.[12]

Among multi-stepped transitions, those of two-step character are the most prevalent in the literature and can be realised

aSchool of Chemistry, The University of Sydney, NSW, 2006, Australia. E-mail: suzanne.neville@sydney.edu.au; Tel: +61-2-9351-7791

bX-ray Science Division, Advanced Photon Source, Argonne National Laboratory, IL 60439, USA

cCNRS, Univ. Bordeaux, ICMCB, UPR 9048, F-33600, Pessac, France

† Electronic supplementary information (ESI) available: Characterisation of materials. CCDC 1038403–1038407. For ESI and crystallographic data in CIF or other electronic format see DOI: 10.1039/c6sc03114e

through the presence of numerous crystallographically distinct SCO-active sites (*i.e.* [HS–HS] ↔ [HS–LS] ↔ [LS–LS]), a single site with short-range or lower dimensional ordering (*i.e.* [HS] ↔ [HS/LS] ↔ [LS]),[13–17] or long-range ordering, in which a mid-temperature phase transition leads to a distinction between previously equivalent sites (*i.e.* [HS] ↔ [HS–LS] ↔ [LS]).[18–23] Spin transitions proceeding *via* three or more steps are extremely uncommon[24–27] and many examples are poorly structurally characterised compared to two-step materials. The fractional changes in multi-stepped transitions intrinsically require that more complex arrangements of SCO centres establish structural ordering, with the mismatch in coordination bond distances for the LS and HS states imparting significant lattice strain. Notable multi-step examples include the 3-D Hofmann material $[Fe(dpsme)Pt(CN)_4] \cdot (guest)^{[25]}$ (dpsme = 4,4′-di(pyridylthio)methane), which shows formal tristability at fixed temperatures due to overlapping thermal hysteresis of the multi-step transitions and, more recently, an incomplete Devil's staircase-like transition in a 2-D coordination polymer,[26] and a four-step transition in a Hofmann-like phase.[27] In this article, we present a rare four-stepped transition in a family of 2-D Hofmann-type materials which is enabled by a synergy between covalent lattice cooperativity and a network of antagonistic host–host and host–guest interactions. Using the elastic frustration present in the $[FePt(CN)_4]$ planes,[12] combined with axial monodentate ligands able to generate weak interactions between each other or with inserted guest molecules, multiple symmetry breaking alongside spin crossover has been achieved.[13,28,29] The flexibility of the 2-D lattice, combined with the array of interactions, allows the lattice to accommodate five

distinct spin state profiles upon temperature variation. The fractional HS and LS states stabilised here are uniquely related to sixths and present an additional advance toward the theoretical Devil's staircase concept which was recently highlighted for SCO systems to describe the series of steps possible in multi-stepped transitions.[26]

Results and discussion

Overall structure

Single crystal diffraction data were collected on 1^{Pd} and 1^{Pt} at 240 K, representative of the HS Fe(II) state, and revealed isostructural materials; henceforth, the structure of 1^{Pt} will be discussed (Tables S1 and S2†). Overall, the asymmetric unit consists of two unique Fe(II) sites ($\frac{1}{2}$**Fe1** : 1**Fe2**; the $\frac{1}{2}$: 1 ratio arises due to the former lying on an inversion centre whereas the latter is on a general position), one and a half $[Pt(CN)_4]^{2-}$ groups, three unique saltrz ligands, and four water molecules (Fig. S4†), thus giving an overall formula of $[Fe_3^{II}(saltrz)_6(Pt^{II}(CN)_4)_3] \cdot 8(H_2O)$. The distorted octahedral Fe(II) centres are each comprised of four equatorially coordinated $[Pt(CN)_4]^{2-}$ metallo-ligands bound through the N-atoms and two axially coordinated N-donor terminal saltrz ligands; this is typical of Hofmann materials. Two-dimensional Hofmann layers of composition $[Fe^{II}Pt(CN)_4]$ are thus generated through the bridging of Fe(II) sites by four coordinating $[Pt(CN)_4]^{2-}$ units (Fig. 1(a)), with the octahedral Fe(II) geometry completed axially by bound saltrz ligands (coordinated through N1 of the triazole ring), which protrude above and below the Hofmann layer (Fig. 1(b)). These 2-D layers pack efficiently through the inter-digitation of saltrz ligands from neighbouring layers. A 2-D network is produced with sufficient pore area in the interlayer spacing to accommodate solvent water molecules (Fig. 1(c and d) and 2).

A significant driving force for the distinction of **Fe1** and **Fe2** sites is an extensive network of host–host and host–guest hydrogen-bonding interactions facilitated by the saltrz hydroxyl groups. This array of interactions confers significant intra-Hofmann layer ($[Fe^{II}M(CN)_4]$) distortions and a variety of ligand orientations. In particular, the 2-D $[Fe^{II}M(CN)_4]$ layers, which lie approximately in the ac-plane, show a wave-like undulation highlighted by the relative tilt angle of the Fe(II) octahedron out of the plane and the significant deviation of the Fe–N≡C angles from 180° (Table S3† and Fig. 1(b)). This quantification highlights a major distinction between **Fe1** and **Fe2** sites, whereby the **Fe1** octahedra are more tilted than the **Fe2** octahedra (i.e., **Fe1**–N≡C angles show substantially more deviation from linearity) with respect to a perfectly planar Hofmann layer. Notably, within each 2-D $[Fe^{II}M(CN)_4]$ layer the **Fe1** and **Fe2** sites are distributed in stripes along the a-axis with double ribbons of **Fe2** sites separated by single ribbons of **Fe1** (Fig. 1(a and b)).

Of further structural note in distinguishing **Fe1** and **Fe2**, the three crystallographically unique saltrz ligands differ significantly in their geometry and relative interlayer disposition. In particular, the two possible conformations of the appended hydroxyl groups of the saltrz ligands (cis- and trans- with respect to the bound 1,2,4-triazole nitrogen) are distinctly represented, such that **Fe1** is bound to two cis-saltrz ligands and **Fe2** is bound
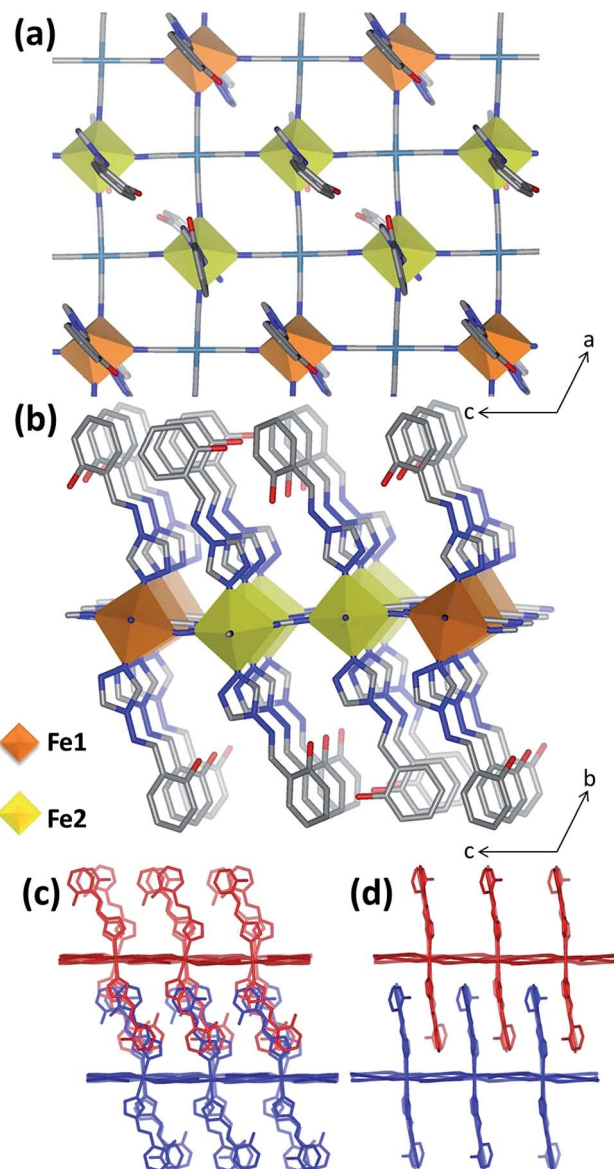

Fig. 1 (a) & (b) Structural representations of 1^{Pt} highlighting where the **Fe1** (orange) and **Fe2** (yellow) sites are positioned within the 2-D Hofmann square grids and the respective saltrz ligand protrusion and geometry above and below the plane. (c) & (d) Illustrations of the interdigitation and efficient packing of two adjacent 2-D Hofmann grids along the b-axis.

to one cis- and one trans-saltrz ligand (Fig. 2). Further distinguishing these ligands is a range of Fe–N–N(trz) 'bite' angles, driven by varying host–host and host–guest interactions (Fig. 2).

Overall, the combination of different octahedral tilt angles of **Fe1** and **Fe2**, respective Fe–N–N(trz) 'bite angles' and cis/trans-conformations results in various ligand 'tilting' within the interlayer spacing (Table S3† and Fig. 2). The most significant consequence of this is the presence of three different spacings between adjacent ligands along the c-axis, labeled as small (S), medium (M) and large (L) in Fig. 2. Within these ligand pair spacings two, one or zero hydroxyl groups protrude. The smaller region (S), despite having ligands in close proximity, does not
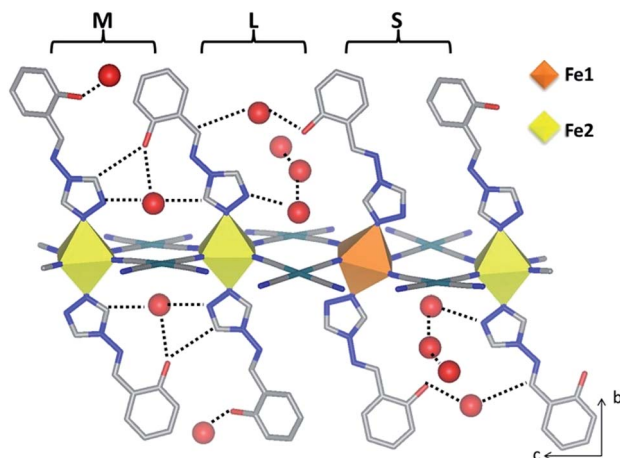
Fig. 2 Structural representation of a single layer of 1^{Pt} showing the array of adjacent saltrz ligand spacings within the interlayer spacing, defined as small (S), medium (M) and large (L). The resultant pores are filled with different amounts of guest water molecules (red spheres) involved in various host–guest and guest–guest interactions as indicated by dotted lines.

display any hydrogen-bonding interactions and, additionally, does not contain any guest water molecules. The medium region (M) contains both host–host and host–guest interactions. The largest region (L) shows numerous host–guest interactions and host–host interactions in the form of a 1-D chain of water molecules along the *a*-direction. This complex array of host–host, host–guest and guest–guest interactions is depicted in Fig. 2 and summarised in Table S5.†

Magnetic susceptibility

Both 1^{Pd} and 1^{Pt} show abrupt and hysteretic four-step SCO character (Fig. 3). Focusing firstly on 1^{Pt} (Fig. 3(a)), with cooling from room temperature, the $\chi_M T$ values remain constant at *ca.* 3.38 cm^3 mol^{-1} K, indicating that all Fe(II) sites are in the HS state. Over the range 215–190 K, a decrease in $\chi_M T$ values is observed followed by a more rapid decrease over the range 190 to 185 K. The step in this region corresponds to a conversion of one-sixth of the HS Fe(II) sites (*i.e.* a resultant 5/6 HS fraction). A plateau with a subtle slope exists over the range 185–160 K. The centre of this plateau region ($\chi_M T = 2.12$ cm^3 mol^{-1} K) represents a conversion of a further one-sixth of the Fe(II) HS sites to the LS state (*i.e.*, overall a 2/3 HS fraction). Over the range 160–150 K the $\chi_M T$ values decrease very rapidly with the $\chi_M T$ values at 150 K corresponding to one half of the remaining HS Fe(II) sites converting to the LS state (*i.e.*, 1/6 HS sites remaining). Below 150 K there is a gradual decrease in $\chi_M T$ values such that all of the Fe(II) sites are in the LS state at temperatures below 90 K (*i.e.*, 0/6 HS fraction). The warming curve shows the same four-step SCO behaviour with hysteresis loops present in the second and third steps (Step 1: $T_{\frac{1}{2}}\downarrow\uparrow$: 200, 202 K; Step 2: $T_{\frac{1}{2}}\downarrow\uparrow$: 190, 194 K; Step 3: $T_{\frac{1}{2}}\downarrow\uparrow$: 156, 162 K; Step 4: $T_{\frac{1}{2}}$: 104 K).

Complex 1^{Pd}, which also displays four-step SCO behaviour, was assessed for photo-excitation properties by irradiating
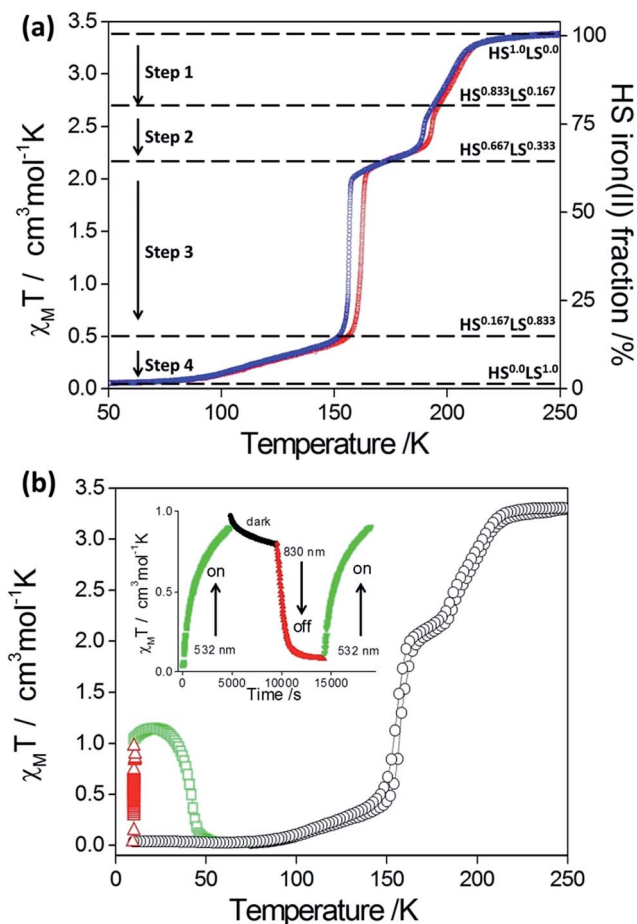

Fig. 3 (a) $\chi_M T$ and HS fraction *versus* temperature for 1^{Pt} (blue: cooling, red: heating) displaying the complete four-step SCO behaviour. Step regions and nHS/HS^{total} for the respective five distinct spin states are indicated. (b) $\chi_M T$ *versus* temperature for 1^{Pd} (black (○): thermal spin transition, red (△): irradiation at 10 K with $\lambda = 510$ nm and green (□): relaxation in the dark showing photo-excitation properties). Inset: reversibility of photo-induced state using alternating 510 nm ('on') and 830 nm ('off') wavelengths.

a thin layer of crystals at 10 K ($\lambda = 510$ nm, Fig. 3(b)). A degree of photo-excitation of the LS species to a metastable HS state was observed, with the $\chi_M T$ product reaching saturation at 1.2 cm^3 mol^{-1} K. This indicates a photo-excitation efficiency of around 30%. The photoactivity process is readily cycled 'on' and 'off' at 10 K with alternating irradiation at wavelengths of 510 nm (LIESST effect) and 830 nm (reverse-LIESST effect) (Fig. 3b (inset)). The T(LIESST) value for 1^{Pd} (42 K) is consistent with other 2-D framework materials containing flexible unidentate ligands (Fig. S7†).[25,29–31] It would be of interest to investigate *via* structural methods if the non-quantitative photo-conversion is related to multi-stepped SCO behaviour, whereby a stoichiometric 2/6 HS fraction step, which was bypassed in the thermal SCO for the bulk sample, could be accessed by irradiation, or whether it is related to the strong competition between relaxation and excitation in this low temperature region.

Variable temperature synchrotron powder X-ray diffraction

As an initial overview of the evolution of the bulk structure *versus* temperature, powder X-ray diffraction analysis was carried out on 1^{Pt} using synchrotron radiation (280–100 K). The overall thermal dependence of the peak positions reflects a four-step SCO transition (Fig. 4(a)). Fine analysis of individual patterns reveals the emergence of additional Bragg peaks over the distinct temperature range 195–150 K, indicative of a phase transition. Fig. 4(b) highlights the region $2\theta = 7$–$7.5°$ where additional reflections (*e.g.* $(1 \; -1 \; -2)$) are present at 250 and 100 K, but absent at intermediate temperatures (*e.g.* 170 K). Thus a different crystallographic phase exists over the temperature regions encompassing Steps 2 and 3 (Fig. 3(a)). This re-entrant behaviour occurs such that the high and low temperature regions display the same unit cell and symmetry separated by a unique 'intermediate' phase.[18] Le Bail analysis of individual patterns (performed using the parent cell parameters) was carried out and maps the thermal dependence of the magnetic susceptibility precisely (Fig. S6†), thus confirming the bulk structure–function behaviour.

Variable temperature single crystal data analysis

In order to correlate the rare four-step SCO behaviour with structural features and the unusual plateau points (*i.e.* at sixths instead of quarters), variable temperature single crystal data were collected at each plateau region in the magnetic data (Table S1†). The following structural analysis is focused on the 1^{Pt} analogue.

With cooling over the range 240 to 195 K, the same crystal symmetry and approximate cell parameters are observed representative of the 'parent cell'. Complete structural analysis at 240 K reveals average Fe–N bond lengths consistent with both Fe(II) sites being in the HS state (Table S3†). At this temperature there are two Fe(II) sites, **Fe1** and **Fe2** present in a 1 : 2 ratio (Fig. 5(a)). The main structural deviations distinguishing these two sites at this temperature are differing degrees of octahedral distortion, octahedral tilt out of the Hofmann layer plane and
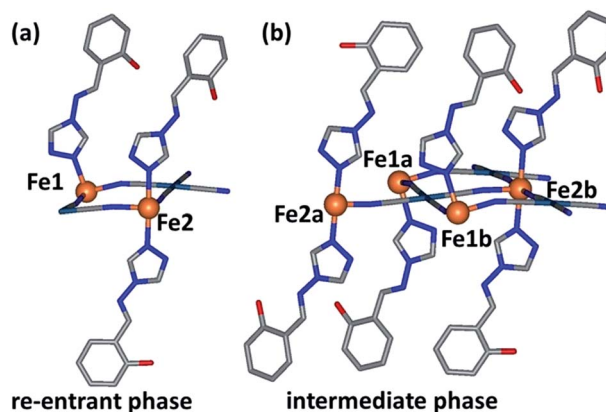

Fig. 5 Asymmetric unit of 1^{Pt} representative of (a) the parent cell (240, 120 and 90 K) and (b) the phase transition cell (192 and 170 K).

relative orientations of saltrz ligands (as discussed above). Importantly for the subsequent SCO properties, we note again that the **Fe1** and **Fe2** sites in this parent phase are distributed within each Hofmann layer in ribbons along the *a*-axis with pairs of **Fe2** ribbons dispersed between single **Fe1** ribbons (Fig. 6(a)).

With further cooling, by 192 K, which represents the Step 1 plateau region, new reflections appear in each of the $(\frac{1}{2}kl)$, $(h\frac{1}{2}l)$ and $(hk\frac{1}{2})$ planes indicative of a three-dimensional unit cell transformation whereby the primitive triclinic symmetry is retained and the unit cell volume less than doubles (Tables S1 and S3†). Consequential to this phase transition, both the **Fe1** and **Fe2** sites split into two further unique sites, **Fe1(a)**, **Fe1(b)**, **Fe2(a)** and **Fe2(b)** such that there are now twice as many crystallographically distinct Fe(II) sites as in the parent cell (Fig. 5(b)). Of relevance to the magnetic properties, the relative ratio of these sites is 1**Fe1(a)** : 1**Fe1(b)** : 2**Fe2(a)** : 2**Fe2(b)**. The **Fe1(a)**, **Fe1(b)**, **Fe2(a)** and **Fe2(b)** sites in this transformed phase are distributed within each Hofmann layer as depicted in Fig. 6(b), whereby there are complete stripes of **Fe1(a)** or **Fe1(b)** chains separated by pairs of **Fe2(a)** and **Fe2(b)** chains, where the two sites alternate along the *a*-axis.

Careful assessment of diffraction images reveals that this new phase is present over the range 192–150 K, representative of Step 2, as observed using powder diffraction. Complete structural analysis at 192 K, representative of the 5/6 HS fraction plateau, indicates that the **Fe1(a)** and **(b)** sites retain an HS character along with the **Fe2(b)** site. The **Fe2(a)** sites show a 0.1 Å decrease in apparent Fe–N bond length indicating a 50 : 50 mixed HS : LS state of short-ranged ordered Fe(II) spin states (Fig. 6(b)). Thus, in this phase there are 5HS and 1LS Fe(II) sites (1**Fe1(a)**^{HS} : 1**Fe1(b)**^{HS} : 1**Fe2(a)**^{HS} : 1**Fe2(a)**^{LS} : 2**Fe2(b)**^{HS}), comprised of long- and short-range ordered spin states, consistent with magnetic measurements and a 5/6 HS fraction.

Structural analysis at 170 K, representative of the 2/3 plateau, reveals that the **Fe2(a)** site converts completely to the LS state as illustrated in Fig. 6(c) (Table S3†). Thus, all Fe(II) sites show long-range ordering of the respective HS and LS states (1**Fe1(a)**^{HS} : 1**Fe1(b)**^{HS} : 2**Fe2(a)**^{LS} : 2**Fe2(b)**^{HS}), with the
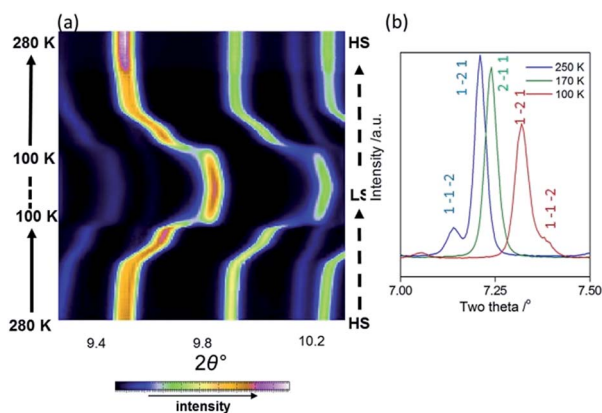

Fig. 4 (a) Variable temperature powder X-ray diffraction of 1^{Pt} (280 – 100 – 280 K), showing the step-wise shift of Bragg peaks mimicking the magnetic data. (b) Representative powder X-ray diffraction images at 250, 170 and 100 K, highlighting a phase transition.
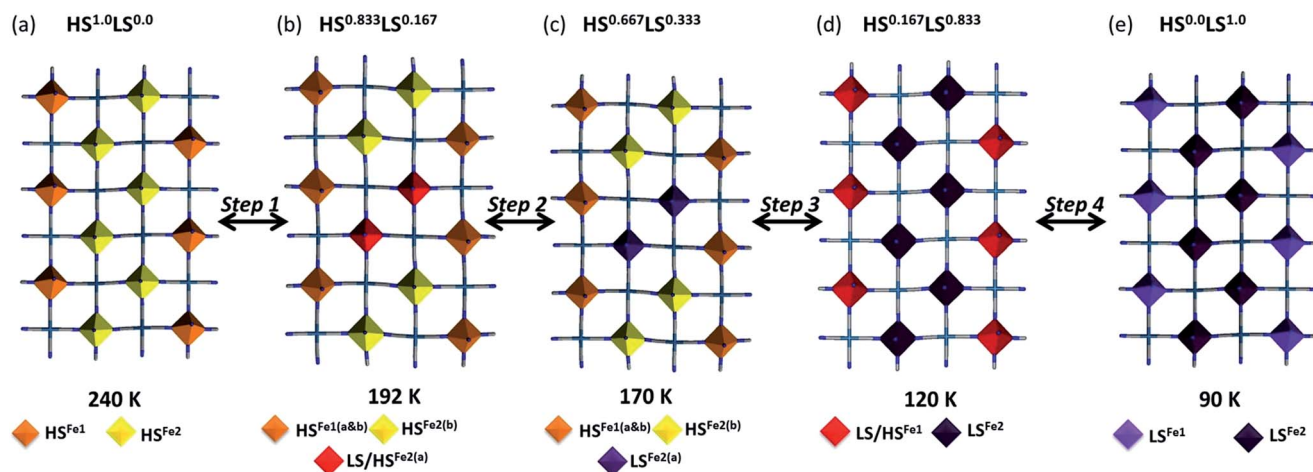
Fig. 6 (a–e) Structural representation of a single Hofmann layer of 1^{Pt} (saltrz ligands removed) indicating the position of HS and LS Fe(II) sites (polyhedra) within each grid over the four step SCO process. Temperature of data collection, relative HS^nLS^{1-n} state represented and Fe(II) spin state indicated.

4HS : 2LS ratio again agreeing with magnetic data at this temperature. During the abrupt spin transition process of Step 3, the additional superstructure reflections associated with the structural modulation diminish, reverting entirely to the parent cell by 150 K. The 'parent cell' is then retained at low temperatures. Structural analysis at 120 K, representative of the 1/6 plateau, reveals that all of the **Fe2** sites convert entirely to the LS state and half of the **Fe1** sites, resolved as a 50 : 50 mixed HS : LS state of short-range ordered Fe(II) spin states (Fig. 6(d) and Table S3†). This is consistent with a 1/6 HS Fe(II) fraction at this temperature ($1\mathbf{Fe1}^{HS} : 1\mathbf{Fe1}^{LS} : 4\mathbf{Fe2}^{LS}$). As per the 5/6 plateau both long- and short-range ordering of Fe(II) spin states are represented. By 90 K, a complete LS character is attained for all Fe(II) sites as depicted in Fig. 6(e) (Table S3†). Thus there are 5 magnetically and structurally distinct states for this material, comprising of a range of long- and short-range ordered Fe(II) spin states and with novel nano-patternings of local spin states.

Magneto-structural rationalisation

It is clear from the unique Fe(II) site distinctions in both the parent and phase transition states why a multi-step behaviour arises that is associated with integer sixth's fractions of HS Fe(II) states, i.e., 3 or 6 unique metal sites are present. What is less evident is why the 5/6, 4/6 and 1/6 states are stabilised in either subtle or distinct plateau regions, whereas other integer sixth fraction states (e.g., 2/6 and 3/6) are bypassed in the very abrupt transition of Step 3.

In general, Fe(II) sites that are in a relatively less distorted octahedral environment will preferentially undergo an HS to LS transition upon cooling. In this case, the local **Fe1** and **Fe2** octahedral environments are in much the same distortive state (Table S3†). Considering that the overall intrinsic cooperativity of Hofmann materials stems from the short cyano-bridges of the Hofmann layer efficiently propagating spin state information, distortions within the layer are likely to play a significant role in stabilising the intermediate lattice states. Indeed,

Hofmann-layer Fe–N≡C angles which are more idealised (i.e., 180°) would provide a favorable spin transition pathway owing to π-back-bonding effects. Indeed, here, the **Fe2**–N≡C angles are distinctly more regular compared to those of **Fe1**, and thus **Fe2** transitions before **Fe1** in the cooling profile. Of course this is a very simplistic rationale as there are evidently many other outer coordination sphere distinctions between **Fe1** and **Fe2** that would contribute to their relative HS stability. In any case, the deviation of these angles appears to only influence the initial onset of SCO and play little role thereafter, remaining essentially constant.

With cooling from the HS state phase, the **Fe1** and **Fe2** sites each distinguish into further unique sites via a single crystal phase transition, resulting in a subtle plateau (of four long-range ordered HS sites and two short-range ordered 'mixed' HS/LS sites) followed by a thermally stable plateau (of four HS sites and two LS sites long-range ordered). The driving force for the phase transition and plateau stabilisation is clear when the resultant octahedral distortions are considered (Table S3†). Of particular note is the increase in octahedral distortion at a number of these sites with cooling despite retaining an HS character (i.e., Step 1: $\Sigma^{\mathbf{Fe1}}$ 18° → $\Sigma^{\mathbf{Fe1(b)}}$: 23.3° and Step 2: $\Sigma^{\mathbf{Fe1(a)}}$ 17.6° → $\Sigma^{\mathbf{Fe1(a)}}$: 26.4°). This effect, termed negative- (or anti-) cooperativity,[13,32,33] which is of antiferro-elastic origin, has been noted previously in systems such as this and dinuclear materials where there are strong coordination pathways between SCO sites. Thus volumetric HS → LS variations of nearby sites are strongly communicated (i.e., lattice cooperativity). As the lattice cannot accommodate these changes, nearby sites must adjust by becoming more irregular, i.e., increased HS stability, thus the term anti-cooperativity is employed to represent antiferro-elastic-like effects. Hence, the Step 1 and Step 2 plateau regions (and the associated phase transition) are enabled by strong lattice cooperativity which results in negative-communication effects and the stabilisation of these sites in the HS state.

A clear feature in the spin transition curve is the abrupt spin state transition of Step 3, which bypasses the potential spin state fractions of 3/6 and 2/6 resulting in a 1/6 HS fractional state. In this step, the **Fe1** and **Fe2(a)** and **(b)** sites, respectively, are no longer crystallographically distinct (*i.e.*, re-entrant phase transition state) and the relative octahedral distortion parameter proceeds in the usual manner. However, it is of note that the **Fe1** site is substantially more distorted at this temperature than at 240 K indicating anti-cooperativity is still a governing factor (*i.e.*, the lattice has not yet obtained energy minimisation). Thus, this abrupt step is facilitated by strong lattice cooperativity, which encourages all of the **Fe2** sites to attain LS character in one step and half of the **Fe1** sites to transition. The fact that both **Fe1** and **Fe2** sites transition in a concerted manner in this step (hence bypassing 3/6 and 2/6 plateau options) further illustrates the efficient lattice cooperativity of this system. Furthermore, it is likely that the distinctly large distortion parameter observed for the **Fe1(a)** site in Step 3 ($\Sigma^{\mathbf{Fe1(a)}}$: 26.4°) inhibits a full conversion of all $Fe(\text{II})$ sites to the LS state in this step. Moreover this relatively distorted site enables thermal stability of this state at relatively low temperatures, such that the Step 4 transition to a completely LS state is only thermally accessible at temperatures below 90 K.

Conclusions

In summary, we have presented a rare example of a four-stepped SCO material enabled by the strategic incorporation of structure directing interaction sites (in particular hydrogen bonding sites) in combination with a framework topology with intrinsic solid state cooperativity. The presence of five structurally distinct spin state phases, encompassing a unique array of short- and long-range ordered $Fe(\text{II})$ spin state arrangements, is directly facilitated by these flexible interactions. In particular, lattice distortions are present and stabilised here by a rich variety of host–host and host–guest interactions with the ligand –OH functional group. As distinct from other Hofmann-type materials displaying multi-step SCO, quite different layer periodicity has been obtained as a direct consequence of using an asymmetric ligand. The fact that the specific spin state patternings achieved here are new indicates that there is not one common series of transitions that the Hofmann layer can undergo. This study highlights that multi-stable electronic switching character is achieved though the presence of lattice distortive interactions; however, the variety of multistep behaviours now reported indicate that there is no common structural facet underlying these frustration effects.

With examples of four-stepped spin transitions being rare, detailed studies encompassing parallel structural and magnetic correlations are essential for fundamental appreciation and to enable future targeted synthetic approaches. Our comprehensive structure–function correlation studies highlight the intrinsic necessity to conduct thorough analysis to completely understand such complex behaviours; most significantly, we would state the importance of conducting structural analyses on both bulk powders and single crystal samples over a broad temperature range to ensure that multi-stepped transitions apparent in magnetic susceptibility measurements are not due to the presence of multiple phases with differing SCO behaviours.

Acknowledgements

Notes and references

1 O. Kahn, *Molecular Magnetism*, VCH, New York, 1993.

2 P. Gütlich and H. A. Goodwin, *Top. Curr. Chem.*, 2004, **233**, 1–47.

3 M. A. Halcrow, *Spin-crossover materials: properties and applications*, John Wiley & Sons, Ltd, 2013.

4 P. Gütlich, A. B. Gaspar and Y. Garcia, *Beilstein J. Org. Chem.*, 2013, **9**, 342–391.

5 P. Gütlich, A. Hauser and H. Spiering, *Angew. Chem., Int. Ed. Engl.*, 1994, **33**, 2024.

6 O. Kahn and C. J. Martinez, *Science*, 1998, **279**, 44–48.

7 J. A. Real, A. B. Gaspar and M. C. Muñoz, *Dalton Trans.*, 2005, 2062.

8 P. Gütlich, Y. Garcia and T. Woike, *Coord. Chem. Rev.*, 2001, **219–221**, 839.

9 J. A. Real, A. B. Gaspar, V. Niel and M. C. Muñoz, *Coord. Chem. Rev.*, 2003, **236**, 121–141.

10 J.-F. Létard, P. Guionneau and L. Goux-Capes, *Top. Curr. Chem.*, 2004, **235**, 221–249.

11 M. Halcrow, *Chem. Soc. Rev.*, 2011, **40**, 4119–4142.

12 M. Paez-Espejo, M. Sy and K. Boukheddaden, *J. Am. Chem. Soc.*, 2016, **138**, 3202–3210.

13 Y. M. Klein, N. F. Sciortino, F. Ragon, C. E. Housecroft, C. J. Kepert and S. M. Neville, *Chem. Commun.*, 2014, **50**, 3838–3840.

14 J. J. Amoore, C. J. Kepert, J. D. Cashion, B. Moubaraki, S. M. Neville and K. S. Murray, *Chem.–Eur. J.*, 2006, **12**, 8220–8227.

15 S. M. Neville, B. A. Leita, G. J. Halder, C. J. Kepert, B. Moubaraki, J.-F. Létard and K. S. Murray, *Chem.–Eur. J.*, 2008, **14**, 10123–10133.

16 Y. Garcia, O. Kahn, L. Rabardel, B. Chansou, L. Salmon and J. P. Tuchagues, *Inorg. Chem.*, 1999, **38**, 4663–4670.

17 J. Tnag, J. S. Costa, S. Smulders, G. Molnár, A. Bousseksou, S. J. Teat, Y. Li, G. Albada, P. Gamez and J. Reedijk, *Inorg. Chem.*, 2009, **48**, 2128–2135.

18 D. Chernyshov, M. Hostettler, K. W. Törnroos and H.-B. Bürgi, *Angew. Chem., Int. Ed.*, 2003, **42**, 3825–3830.

19 S. Bonnet, M. A. Siegler, J. S. Costa, G. Molnár, A. Bousseksou, A. L. Spek, P. Gamez and J. Reedijk, *Chem. Commun.*, 2008, 5619–5621.

20 M. Griffin, S. Shakespeare, H. J. Shepherd, C. J. Harding, J.-F. Létard, C. Desplanches, A. E. Goeta, J. A. K. Howard, A. K. Powell, V. Mereacre, Y. Garcia, A. D. Naik, H. Müller-Bunz and G. G. Morgan, *Angew. Chem., Int. Ed.*, 2011, **50**, 896–900.

21 B. J. Vieira, J. T. Coutinho, I. C. Santos, L. C. Pereira, J. C. Waerenborgh and V. da Gama, *Inorg. Chem.*, 2013, **52**, 3845–3850.

22 D. Boinnard, A. Bousseksou, A. Dworkin, J.-M. Savariault, F. Varret and J.-P. Tuchagues, *Inorg. Chem.*, 1994, **33**, 271–281.

23 C.-F. Sheu, S. Pillet, Y.-C. Lin, I.-J. Hsu, C. Lecompte and Y. Wang, *Inorg. Chem.*, 2008, **47**, 10866–10874.

24 M. Nihei, H. Tahira, N. Takahashi, Y. Otake, Y. Yamamura, K. Sato and H. Oshio, *J. Am. Chem. Soc.*, 2010, **132**, 3553–3560.

25 N. F. Sciortino, K. R. Scherl-Gruenwald, G. Chastanet, G. J. Halder, K. W. Chapman, J.-F. Létard and C. J. Kepert, *Angew. Chem., Int. Ed.*, 2012, **51**, 10154–10158.

26 E. Trzop, D. Zhang, L. Piñeiro-Lopez, F. J. Valverde-Muñoz, M. C. Muñoz, L. Palatinus, L. Guerin, H. Cailleau, J. A. Real and E. Collet, *Angew. Chem., Int. Ed.*, 2016, **55**, 8675–8679.

27 J. E. Clements, J. R. Price, S. M. Neville and C. J. Kepert, *Angew. Chem., Int. Ed.*, 2016, DOI: 10.1002/anie.201605418.

28 R. Otahani, M. Arai, H. Ohba, A. Hori, M. Takata, S. Kitagawa and M. Ohba, *Eur. J. Inorg. Chem.*, 2013, 738–744.

29 V. Martinez, Z. A. Castillo, M. C. Muñoz, A. B. Gaspar, C. Etrillard, J.-F. Létard, S. A. Terekhov, G. V. Bukin, G. Levchenko and J. A. Real, *Eur. J. Inorg. Chem.*, 2013, 813–818.

30 N. F. Sciortino, S. M. Neville, J.-F. Létard, B. Moubaraki, K. S. Murray and C. J. Kepert, *Inorg. Chem.*, 2014, **53**, 7886–7893.

31 S. M. Neville, G. J. Halder, K. W. Chapman, M. B. Duriska, P. D. Southon, J. D. Cashion, J.-F. Létard, B. Moubaraki, K. S. Murray and C. J. Kepert, *J. Am. Chem. Soc.*, 2008, **130**, 2869–2876.

32 S. G. Telfer, B. Bocquet and A. F. Williams, *Inorg. Chem.*, 2001, **40**, 4818–4820.

33 C. M. Grunert, S. Reiman, H. Spiering, J. A. Kitchen, S. Brooker and P. Gütlich, *Angew. Chem., Int. Ed.*, 2008, **47**, 2997–2999.